A Differential Hall Effect method with sub-nanometre resolution for active dopant concentration profiling in ultra-thin Si 1-x Ge x and Si doped layers

Richard Daubriac, Emmanuel Scheid, S. Joblot, R. Beneyton, P Acosta Alba, S. Kerdiles, Fuccio Cristiano

A Differential Hall Effect method with sub-nanometre resolution for active dopant concentration profiling in ultra-thin $Si_{1-x}Ge_x$ and Si doped layers

R. Daubriac*[1], E. Scheid[1], S. Joblot[2], R. Beneyton[2], P. Acosta Alba[3], S. Kerdilès[3], F. Cristiano[1]

Address:

[1]LAAS-CNRS and Univ. of Toulouse, 7 avenue du Colonel Roche, 31400 Toulouse, France.

[2]STMicroelectronics, 850 rue Jean Monnet, 38926 Crolles, France.

[3]CEA-LETI and Univ. of Grenoble, 17 rue des Martyrs, 38054 Grenoble, France.

Email:

Richard Daubriac – richard.daubriac@laas.fr

* Corresponding author

Abstract

In this paper, we present an enhanced Differential Hall Effect method (DHE) for Si and SiGe ultrathin layers for the investigation of dopant activation in the surface region with sub-nanometre resolution. In the case of SiGe case, which constitutes the most challenging process, we show the reliability of the SC1 chemical solution (NH_4OH:H_2O_2:H_2O) thanks to its slow etch rate, stoichiometry conservation and low roughness generation. The reliability of a complete DHE procedure, with an etching step as small as 0.5 nm, is demonstrated on a dedicated 20 nm-thick SiGe test

structure fabricated by CVD and uniformly doped *in situ* during growth. The developed method is finally applied to the investigation of dopant activation achieved by advanced annealing methods (including millisecond and nanosecond laser anneal) in two material systems: 6 nm-thick SiGeOI and 11 nm-thick SOI. In both cases, DHE is shown to be a unique sensitive characterisation technique for a detailed investigation of dopant activation in ultra-shallow layers, providing sub-nm resolution for both dopant concentration and carrier mobility depth profiles.

Keywords

Differential Hall Effect; FDSOI; dopant activation; carrier mobility; sub-nanometre resolution; contact resistance; laser annealing.

Introduction

The research efforts made throughout the last decades have made it possible to keep the momentum for a continuous miniaturization of electronics devices. For instance, the “bulk” planar transistor limitations have been overcome thanks to the transition towards more complex device architectures. These include enhanced planar architectures such as FDSOI [1] or 3D architectures ranging from TriGate FinFETs [2] to gate-all-around NWFETs [3] and Monolithic 3D CoolCube technology [4]. Despite their differences, some technological issues have emerged as a significant challenge for all of them, such as the need to reduce the contact resistance at the silicide/source-drain interface [5].

The increase of the active dopant concentration at the surface of the source/drain material (usually Si or SiGe) is a strong lever for access resistance reduction [6], and several process solutions have been proposed to this purpose, involving advanced implant or annealing techniques [7]. Within this context, the optimization of existing characterisation techniques for the measurement of dopant activation at the

semiconductor surface (or the development of new ones) is therefore decisive for both the improvement of the fabrication processes and the calibration of the related TCAD physical models.

For device architectures based on planar SOI substrates (such as FDSOI or 3D CoolCube), measurements of active dopant concentrations from “blanket wafer” experiments are still relevant for process and TCAD optimisation, which are in principle achievable thanks to several known 1D measurement techniques previously developed for dopant profiling. However, in the case of contact resistance optimisation, only the dopant concentration close to the surface is relevant (i.e. within the first few nm), while the SOI/SiGeOI substrates used in current technologies are extremely thin (top layer < 10 nm), making it necessary to dispose of a measurement techniques with sub-nm resolution. For this reason, 1D techniques based on small angle bevel preparation (such as Spreading Resistance Profiling (SRP) [8] or Scanning Capacitance Microscopy (SCM) [9,10]) become extremely difficult to implement and control in view of such a small resolution. Thanks to the use of an AFM tip, 2D Scanning Spreading Resistance Microscopy (SSRM) has been shown to achieve sub-nm resolution [11,12]. However, in this technique, the carrier concentration is inferred from resistivity profile under the assumption that carrier concentration varies ideally with mobility, which is not always the case, especially when part of the dopant is not electrically active [13]. Finally, capacitance-based techniques such as SCM or Electrochemical Capacitance Voltage (ECV) [14], provide reliable values of carrier concentrations only in the absence of additional electrically active defects, which can affect the CV signal [15]

On the contrary, Differential Hall Effect (DHE) profiling [16,17] can potentially meet all the requirements related to the precise measurement of dopant activation at the semiconductor surface. DHE relies on the iteration of etching process and

conventional Hall effect measurements. The active carrier profile is therefore measured without any assumption on the magnitude of the carrier mobility. In addition, measurements are made by stripping the material in successive steps rather than bevelling the surface. The depth resolution of the final dopant concentration profile is therefore defined by the etch rate and indeed nanometric resolution has been successfully demonstrated for Si and Ge, applying oxidation processes like anodisation [18] or oxidising chemistry [19-22]. Nevertheless, etching SiGe alloys with nanometric resolution is far more challenging considering that Si and Ge have different oxidation rates [23]. For this reason, reliable DHE measurements of doped SiGe layers are not available in literature. Finally, in all published DHE investigations, the removal rate is assumed to stay constant, however, even small variations in the removed thickness among nominally identical etch steps can strongly distort the final carrier concentration and mobility profiles.

In this paper, we present an enhanced Differential Hall Effect method that allows to precisely determine the level of dopant activation close to the semiconductor surface for Si and SiGe. First, we detail the etching processes that we have developed for each semiconductor, with particular focus to the SiGe case, which constitutes the most challenging process. For both materials, our method include a direct measurement of the removed thickness after each removal step, so to avoid averaging the etch rate and improve the depth resolution. Then, we demonstrate the reliability of a complete DHE procedure on a dedicated SiGe test structure fabricated by CVD and uniformly doped *in situ* during growth. Finally, we will apply our DHE method to the investigation of dopant activation achieved by advanced annealing methods in two material systems: 6 nm-SiGeOI and 11 nm-SOI.

Description and validation of etching processes for $Si_{1-x}Ge_x$ and Si

Etching process for $Si_{1-x}Ge_x$

Different methods have been proposed in literature for the controlled etch of SiGe layers [24-26]. We first analysed the main characteristics of each solution in terms of the specific requirements related to their application for DHE measurements. In particular, *(i)* the solution must etch Si and SiGe simultaneously so that the SiGe stoichiometry is not modified; (*ii)* the solution must be strongly selective with respect to Si so to preserve the surrounding Si areas in Van der Pauw test structures; *(iii)* the solution must be chemically active for a relatively long period (~1 day) so to be used for several "etch and measurement" cycles; *(iv)* the etch rate must be slow (~1 Ang./min) to allow for sub-nm resolution. Taking into account the above mentioned criteria, we therefore selected the one-step chemistry based on SC1 (NH_4OH:H_2O_2:H_2O 1:1:5) which oxidizes and dissolute at the same time both.

We then investigated the efficiency of the SC1 solution by running several tests as a function of different experimental parameters (time, temperature, Ge content, etc…). For this, spectroscopic ellipsometry (with a HORIBA Jobin Yvon system) was used as a fast, reliable and non-destructive method for the measurement of the removed thickness. We developed an empirical model for the quantification of the SiGe thickness measurement (based on a SiGe/Si two layers stack and a point-by-point calculation procedure), which was calibrated using other techniques (such as TEM and XRD). As an example, **Figure 1** summarizes the removed thickness measured by XRD (in (004) configuration), bright field high resolution TEM and ellipsometry as a function of etching time from a 20 nm-thick $Si_{0.73}Ge_{0.27}$ boron-doped layer (10^{18} at.cm^{-3}) grown on top of a Si substrate.

TEM images show a clear decrease of the layer thickness, while all the techniques are in mutual agreement, therefore validating the ellipsometry as a unique thickness characterization method for the remainder of this work.

From this study we estimated a value of 0.95 Å/min for the etchrate of the SC1 solution on $Si_{0.73}Ge_{0.27}$, without any alteration of the layer original stoichiometry, as confirmed by XRD analysis (cf. **Supporting Information File 1**). Moreover, the found etchrate is in very good agreement with previous results obtained by our research group [26]. Concerning the surface roughness, tapping mode AFM analysis provided arithmetic averages R_a of about 1.2 Å (cf. **Supporting Information File 2**).

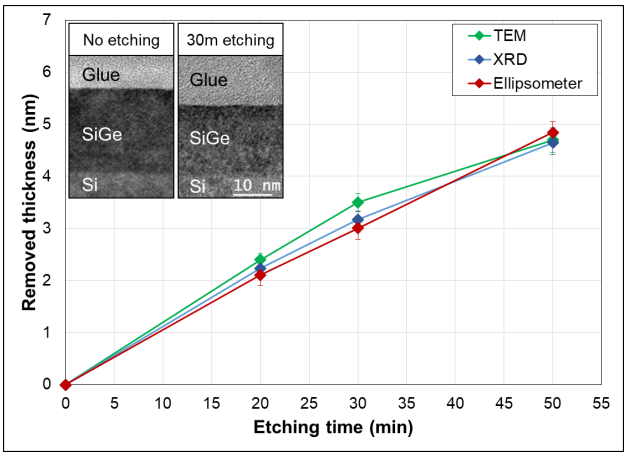

Figure 1: Removed SiGe thickness measured by different methods (TEM, XRD and ellipsometry) as a function of etching time. Ge content: 0.27 at. %. Inset: TEM cross-section micrographs from reference and 30-min etched sample. This figure illustrates the agreement between the three chosen techniques.

However, in view of its application for DHE experiments, it is necessary to use an encapsualtion cell to protect metallic contacts of the electric test structures during etch (cf. **Supporting Information File 3**). Due to the funnel-shaped cell designed for this study, the reaction zone is confined, which results in a reduction of the etchrate. By optimising the experimental set up (use of a magnetic stirrer combined with an

appropriate cell orientation in the solution bath), we managed to limit the etchrate reduction and similar values to “blanket” samples experiments were found. Finally, we investigated the impact of the Ge content on the measured etchrate. Results are shown in **Figure 2**, where we compare the removed thickness as function of etching time for two 20nm boron doped (10^{19} at.cm^{-3}) $Si_{1-x}Ge_x$ with different germanium content : x=0.22 and x=0.3. For etching times lower than 15 minutes, the etchrate is perfectrly linear and independent of the Ge content, with a removed thickness of ~1 nm after 15 minutes. It is therefore possible to use this solution to achieve sub-nm resolution. In summary, all these investigations confirm the choice of SC1 as chemical solution for SiGe etching thanks to its slow etchrate, stoichiometry conservation and low roughness generation.

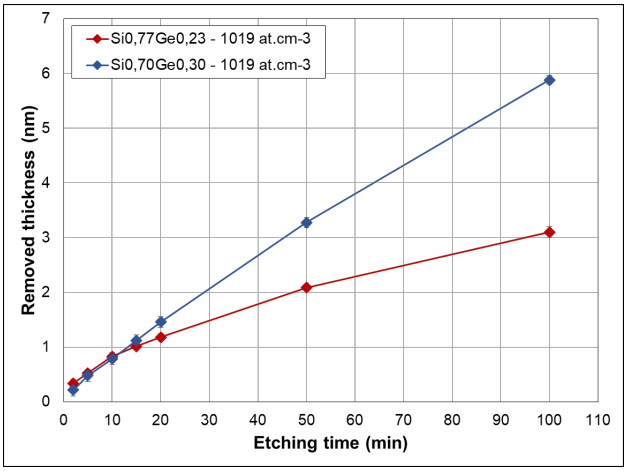

Figure 2: Removed SiGe thickness (measured by ellipsometry) as a function of etching time for two different Ge contents. After the first 15 minutes, the etch rate increases with Ge content.

Etching process for Si

Silicon etching process differs from the SiGe case as it involves a two steps mechanism: first, oxidation then oxide stripping. In this case, the etchrate is not defined as a function of the etching time, but is given by the removed thickness per

step, i.e. the removed thickness between two stripping processes. Resolution of about 1 nm have been obtained in the study of Ling et al [21] combining dilute HF, ultrapure water rinsing and re-oxidation in clean room environment. However, with the aim of minimising the surface roughness, we used ethanol instead of ultrapure water as rinsing solvent [27]. We performed multiple cycles of etching processes on *in situ* boron-doped Si layers (grown on top of Si substrates) with continuous monitoring of the removed thickness (by ellipsometry measurements) and the surface roughness (by AFM characterization). Our results show a sub nanometre cycle by cycle etchrate and a 1 Å final roughness.

DHE procedure validation on SiGe layers fabricated by CVD

In this section, we detail a complete DHE procedure using a 20 nm-thick boron doped at 10^{19} at/cm^3 $Si_{0.77}Ge_{0.23}$ layer grown by CVD on top of Si substrate. We first describe the Van der Pauw structure and the conventional Hall effect setup. Then we will present the differential Hall effect measurements and calculations and we will discuss the limitations of the technique.

Van der Pauw structure and Hall effect measurements on ultra-thin layers

Hall effect measurement is a well-known technique that allows to access three important physical parameters for material characterization: the sheet resistance R_s, the active Hall dose N_H and the Hall mobility μ_H. At first, a Van der Pauw technique is used to determine the sheet resistance, then a magnetic field is applied orthogonally to the sample surface to measure the sheet Hall coefficient R_{SH}, which is finally used to deduce N_H and μ_H.

Several classical Van der Pauw shapes were tested to perform electrical measurements (square, greek cross and bridge “bar shaped” structures). Greek cross shaped test structure has been chosen as it has more advantages than other shapes (cf. **Supporting Information File 4**). First, it provides a less than 1% error on both sheet resistance and Hall coefficient measurements [28-31]. Moreover, it has highly symmetrical shape with peripheral contacts separated from the centre region, in which the current lines converge allowing precise characterization. For this last reason, we were able to design an encapsulation cell (cf. **Supporting Information File 3**) defining a reaction region in the centre part of the greek cross structure while protecting the metallic contacts with the lowest impact on structure symmetry and measurements reproducibility.

Electrical measurements were carried out with a HL5500PC Nanometrics Hall bench equipped with a 0.3T magnet. For each investigated sample, the sheet resistance and the Hall coefficient were measured for several values of the injected current (from 1 μA to 1 mA), and the average values were determined within the current interval exhibiting the most stable measurements (cf. **Supporting Information File 5**), so to keep the experimental errors close to 0.1%.

Scattering correction must be accounted for when extracting Hall effect parameters. Measured values of Hall carrier concentration and Hall mobility are therefore corrected by using the Hall scattering factor, r_H, [32-34] that depends on the studied material (i.e. Ge content, doping type and concentration…). For this study, we used a set of dedicated test samples consisting of 20 nm-thick epitaxially grown Si and SiGe layers, *in situ* doped with Boron (from $1x10^{18}$ cm^{-3} to $1x10^{20}$ cm^{-3}). By comparing experimental Hall values with average calculated values based on the dopant concentration profiles measured by SIMS, we determined a scattering factor of 0.75 for holes in Si and values ranging from 0.4 to 0.35 for holes in SiGe we a Ge content

of 22 at.% and 30 at/%, respectively, in perfect agreement with literature (**Supporting Information File 6**) [32-34].

Some other possible limitations should be considered in view of the implementation of a DHE methodology on ultra-shallow layers. One is quantum confinement, which has been shown to induce band modifications in ultrathin SOI layers with thickness close to ~3 nm [35]. However, the SOI and SiGeOI layers to be investigated in this work will have a minimum thickness of ~6 nm, so that the quantum confinement effect can be neglected. An additional low-dimension effect is the dielectric confinement, which has been investigated in silicon nanowires surrounded by a dielectric material (such as its native oxide) [36,37]. For nanowire diameters in the ~10 nm range, a dopant deactivation is observed due to the dielectrical mismatch between the silicon and its surroundings. However, our previous investigations on 5 nm-thick SiGeOI layers doped by ion implantation and activated by conventional annealing techniques (RTA) [38,39] indicated a perfect correlation between measured activation and simulated activation, suggesting that dielectric confinement affects more significantly 3D than 2D structures at low dimensions.

Finally, when quantifying the active dopant and mobility depth profiles with DHE, the surface depletion effect should be considered [40,41]. This results from carriers becoming trapped in surface states and can lead to a depletion of carriers below the surface. As a consequence, the DHE profile might require a correction (depth scale translation) corresponding to the depletion width. And in the case of non-uniform doping profiles, the depletion width (and the related correction) will vary with depth. Fortunately, for high carrier concentrations as those investigated in this work, the extent of depletion becomes small and can be neglected. Indeed, for a 10^{19} at/cm^3 doping concentration, and considering typical silicon dioxide charge densities

between 10^{10} and 10^{12} cm^{-2} eV^{-1}, the surface depletion is well below 1 nm, and the surface depletion effect can therefore be neglected.

Differential Hall Effect data measurements and limitations

We performed a full set of DHE measurements on a 20nm-thick $Si_{0.77}Ge_{0.23}$ layer grown by CVD on top of Si a substrate and uniformly doped with boron at 10^{19} at.cm^{-3} (**Supporting Information File 7**). The layer was verified to be fully electrically active. A first run of six etch cycles (15 minutes each) was initially performed. The sample was then kept for three days in a clean room environment. Then, a second run of three etch cycles was carried out. Both runs were initiated without removing the initial native silicon dioxide. Electrical parameters R_S, N_H and μ_H are reported in **Figure 3** as function of etching time. Error bars are not reported as variations for each measured parameter are close to 0.1% (cf. **Supporting Information File 5**).

Two different behaviours are observed: on the one hand, the mobility stays constant with no discontinuity throughout the two measurement runs; on the other hand, the sheet resistance R_S constantly increases (while the Hall dose N_H decreases) and exhibits a discontinuity between the two runs. Indeed, as the doping concentration is uniform throughout the doped layer, the associated carrier mobility is expected to remain invariant in the entire layer. On the contrary, as the layer becomes thinner and thinner, the Hall active dose decreases, and, for fixed carrier concentration (and hence mobility), the increase of the sheet resistance is predicted by **equation (1)**.

$$R_S = \frac{1}{q\int_0^{X_j} C(x).\mu(x).dx} \qquad (1)$$

with X_j being the layer thickness, q the electronic charge, $n(x)$ the dopant concentration as a function of depth and $\mu(x)$ the corresponding mobility profile. The quasi-linear evolution of both R_S and N_H is therefore due to the combination of a

uniform concentration profile and a constant etching time intervals. Concerning the observed discontinuities, it must be considered that a native oxide regrowth occurs between the last measurement of the first run and the first measurement of the second. This regrowth reduces the SiGe thickness by ~1 nm (as measured by ellipsometry) which results in a sheet resistance increase and a Hall active dose decrease, without influencing the mobility.

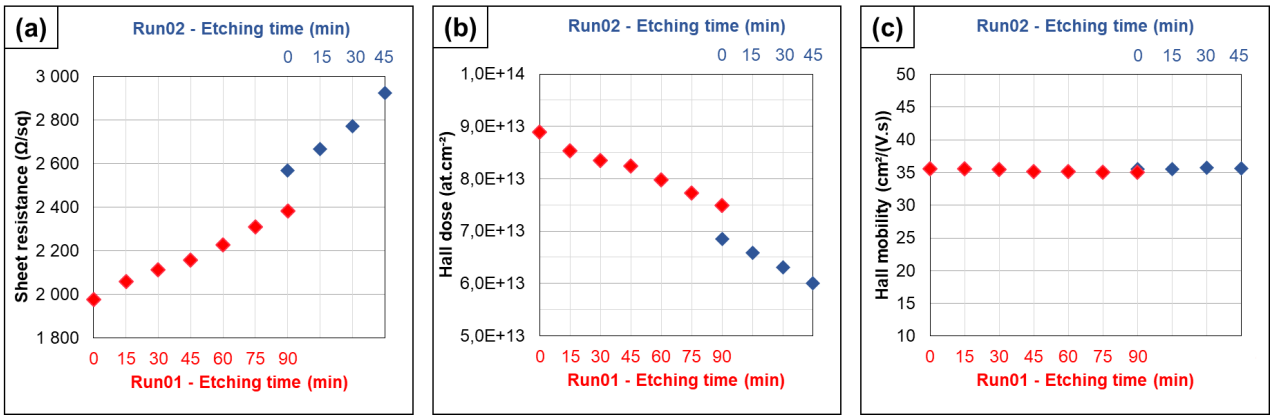

Figure 3: Sheet resistance R_S **(a)**, Hall dose N_H **(b)** and Hall mobility μ_H **(c)** as function of etching times for a 20 nm-thick SiGe layer (x_{Ge}: 0.23 at. %) grown by CVD and *in situ* doped with Boron.

Starting from these raw data, it was finally possible to calculate the differential values of the active concentration and mobility as function of depth. For the *i-th* etched layer, the calculated valus are defined by the following equations [16].

$$n_{DHE_i}\left(x+\frac{\Delta x_i}{2}\right)=\frac{r_H}{q\Delta x_i}\frac{\left(\Delta(\sigma_S)_i\right)^2}{\Delta\left(R_{SH}\sigma_S{}^2\right)_i} \qquad (2)$$

$$\mu_{DHE_i}\left(x+\frac{\Delta x_i}{2}\right)=\frac{\Delta\left(R_{SH}\sigma_S{}^2\right)_i}{r_H\Delta(\sigma_S)_i} \qquad (3)$$

with :

$$\sigma_S = 1/R_S$$
$$\Delta x_i = x_{i+1} - x_i$$
$$\Delta(\sigma_S)_i = \sigma_{S_{i+1}} - \sigma_{S_i}$$
$$\Delta\left(R_{SH}\sigma_S^{\,2}\right)_i = \left(R_{SH}\sigma_S^{\,2}\right)_{i+1} - \left(R_{SH}\sigma_S^{\,2}\right)_i$$

where the conductivity σ_S is given by inversing the found values of the sheet resistance R_S, and R_{SH} is the sheet Hall coefficient used to extract the Hall dose and carrier mobility for each measurement. The term Δx_i corresponds to the removed thickness after each etching process, which is determined by ellipsometry.

From **equations (2)** and **(3)**, DHE active dopant concentration and mobility profiles are finally deduced and reported in **Figure 4 (a)** and **(b)**, respectively (red diamonds). The active dopant concentration profile is compared in **Figure 4 (a)** with the chemical dopant profile measured by SIMS (blue dots), while blue solid lines represent the possible error (± 12,5%) on the SIMS concentration values quantified from standards. It has to be noted that the SIMS signal in the first nm below the surface is affected by measurement artefacts and cannot be considered as fully reliable. Also, at the beginning of each of the two measurement runs, the presence of a native oxide at the sample surface may result in a different surface electrostatic configuration compared to all other cases where the electrical measurements are performed just after the SC1 etching step. This is probably responsible for the upper shift of the calculated concentrations at the surface (first point in **Figure 4 (a)**) and at a depth of 3.5 nm. Overall, **Figure 4 (a)** shows a very good correspondence between the SIMS and the DHE profiles, in perfect agreement with the full electrical activation of the doped layer. More importantly, we show that the SC1 chemistry allowed us to achieve a depth resolution of ~0.5 nm.

Horizontal error bars on DHE values are solely related to the uncertainty of the thickness measurements done by ellipsometry. Indeed, by performing ellipsometry

measurements after each removal step, any possible source of errors related to etchrate variation during the experiment can be neglected. Vertical error bars values are the DHE mobility and dopant concentration uncertainties ($S_{\mu DHE}$ and S_{nDHE}, respectively) calculated assuming R_{SH}, σ_S (and the product $R_{SH}.\sigma_S^2$) as independent variables:[16]

$$S_{\mu_{DHE}} = \left[2.\alpha_2^{\,2}.\left(S_{R_{SH}}^{\,2} + 4.S_{\sigma_S}^{\,2}\right) + 2.\alpha_1^{\,2}.S_{\sigma_S}^{\,2}\right]^{\frac{1}{2}} \qquad (5)$$

$$S_{n_{DHE}} = \left[2.\alpha_2^{\,2}.\left(S_{R_{SH}}^{\,2} + 4.S_{\sigma_S}^{\,2}\right) + 8.\alpha_1^{\,2}.S_{\sigma_S}^{\,2}\right]^{\frac{1}{2}} \qquad (6)$$

with:

$$\alpha_1 = \frac{\sigma_S}{\Delta\sigma_S} \qquad (7)$$

$$\alpha_2 = \frac{R_{SH}\sigma_S^{\,2}}{\Delta\left(R_{SH}\sigma_S^{\,2}\right)} \qquad (8)$$

$$S_{R_{SH}} = \frac{100}{\left|\overline{R_{SH}}\right|}\sqrt{\frac{1}{n-1}\sum_{i=1}^{n}\left(\overline{R_{SH}} - R_{SHi}\right)} \qquad (9)$$

$$S_{\sigma_S} = \frac{100}{\left|\overline{\sigma_S}\right|}\sqrt{\frac{1}{n-1}\sum_{i=1}^{n}\left(\overline{\sigma_S} - \sigma_{Si}\right)} \qquad (10)$$

S_{RSH} (eq. 9) and $S_{\sigma S}$ (eq. 10) represent the relative standard deviation of R_{SH} and σ_S calculated in the range of stability (cf. **Supporting Information File 5**). It is interesting to note that for a chosen etching time interval (i.e. for a chosen depth resolution), α_1 (**equation (7)** and α_2 **equation (8)**) are fixed. As a consequence, $S_{\mu DHE}$ and S_{nDHE} can only be reduced by minimising S_{RSH} and $S_{\sigma S}$, in other words, by obtaining highly reproducible measurements of R_{SH} and σ_S. One must therefore consider the importance of having reproducible measurements when performing DHE data reconstruction. Indeed, for a depth resolution of ~0.5 nm (as the one shown in

Figure 4), a targeted uncertainty of ~15% for μ_{DHE} and n_{DHE} requires that R_{SH} and σ_S must be measured with a relative standard deviation lower than 0.1 %.

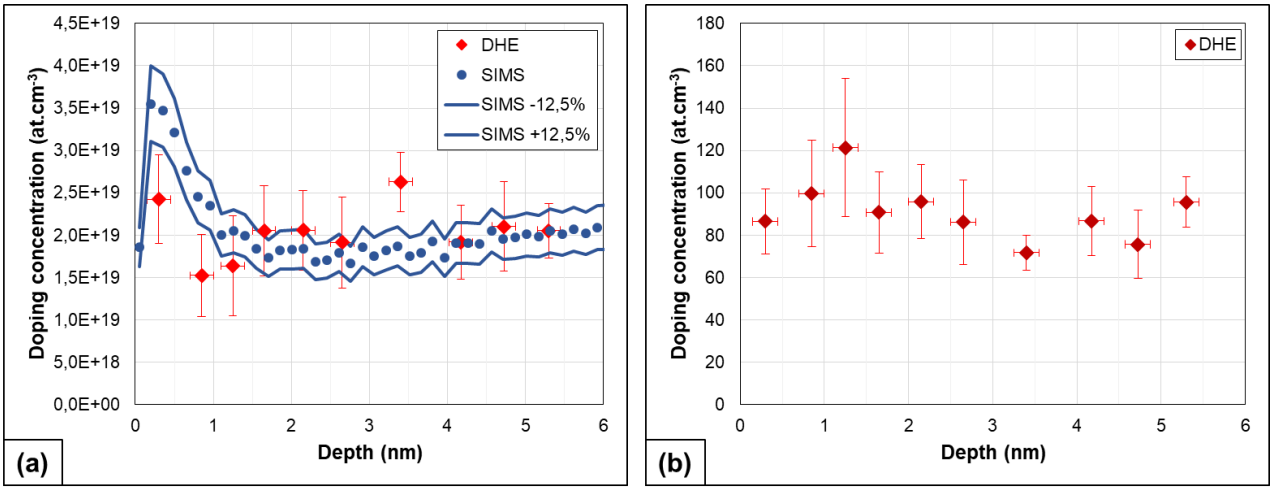

Figure 4: Active dopant concentration **(a)** and carrier mobility **(b)** depth profiles as extracted by DHE method for $Si_{0.77}Ge_{0.23}$ uniformly boron doped at 10^{19} at.cm^{-3}. The active dopant concentration profile is compared in **(a)** with the Boron chemical concentration profile as measured by SIMS.

Within the experimental errors discussed above, the DHE mobility profile reported in **Figure 4 (b)** gives a constant value of the mobility in the first five nanometres, in perfect agreement with the uniform nature of the concentration profile. The average value obtained with calculated DHE points (with an etching step as small as 0.5 nm) is 91.02 ± 13.08 cm^2/(V.s), again in agreement with the more precise value of 88.60 ± 0.27 cm^2/(V.s) that can be extracted from the raw mobility data (cf. **Figure 3c**, r_H = 0.4) obtained from much thicker layers (between 15 and 20 nm-thick). Also, these mobility values are perfectly compatible with those predicted by analytical models for a doping concentration varying between 1x10^{19} cm^{-3} (86 cm^2 / V·s) and 2x10^{19} cm^{-3} (74 cm^2 / V·s) with x_{Ge}=0.23 at T=300K according to the following expression (**equation (11)**): [42]

$$\mu_{TCAD} = \mu_{\min 1}.\exp\left(\frac{-p_C}{N}\right) + \frac{\mu_{const} - \mu_{\min 2}}{1+\left(\frac{N}{C_r}\right)^{\alpha}} - \frac{\mu_1}{1+\left(\frac{C_s}{N}\right)^{\beta}} \quad (11)$$

with:

$$\mu_{const} = \mu_{\max}.\left(\frac{T}{T_o}\right)^{-\gamma}$$

Considering the possible lack of precision in the Ge content of the layer as well as the sub-nanometric depth resolution achieved in these measurements, we can therefore conclude on the good consistency of the DHE method we have developed for SiGe investigation.

Study of 6nm boron-doped SiGeOI layer

Within the recent development of the 3D-sequential integration technology at CEA-LETI, laser annealing is being investigated as a low thermal budget solution for achieving dopant activation in the top transistor level without degrading the performances of the transistors located at the bottom [38]. The efficiency of this technique has already been proven for electrical activation of phosphorus in 22 nm thick SOI structures [43]. In this section, we extend the investigation to SiGeOI layers of 6 nm. Due to the extreme thin size of the layer and the buried oxide, classical 4PP characterization is not possible because of probe penetration down to the substrate. Thanks to Van der Pauw test structure, probe penetration has been circumvented, while conventional and differential Hall effect described in previous sections have been used to investigate dopant activation in laser annealed ultra-thin SiGeOI layers.

Experimental details

The starting SiGeOI wafer has a SiGe top layer of 6 nm and a 20 nm-thick buried oxide (BOX). First step consists in a 3nm Si_3N_4 deposition directly followed by Ge^+ implantation to preamorphise a part of the SiGe crystal and a B^+ implantation for p-

type doping. In the following step, a second Si_3N_4 of 3 nm is deposited prior to laser thermal annealing (LTA). LTA was performed by SCREEN-LASSE using a XeCl excimer laser (λ = 308 nm) with a pulse duration of approximately 160 ns. Finally, several 18x18 mm^2 areas where irradiated with energy densities ranging from 0.65 to 0.79 J/cm^2 (**Supporting Information File 8**).

Structural and conventional Hall effect analysis

Before engaging Hall effect analysis, we consider the structure of the layer before LTA. TEM cross section observations (cf. **Supporting Information File 9**) indicate that the top crystalline SiGe layer has a thickness between 5 and 6 nm, i.e. very close to the original thickness of 6 nm. Indeed, high resolution images show that the layer thickness can rapidly vary by up to 4 lattice planes (i.e. ~1 nm) within few nanometers. This suggests that the Ge PAI implant in this wafer results in a damaged SiGe surface (locally amorphising it) but was not enough to produce a continuous amorphous layer.

Then, we compare electrical parameters measured by conventional Hall effect with the evolution of the crystal structure imaged by TEM as function of laser energy densities. The TEM analysis (cf. **Supporting Information File 10**) shows that for energies of 0.74 and 0.76 J/cm^2, the observed structure is identical to that found in the as-implanted sample with the SiGe layer being almost fully crystalline (and a surface roughness of about 1 nm). This suggests that the laser energy density used in these cases is always lower than the threshold value necessary to melt the surface. In contrast, following a LTA at 0.79 J/cm^2 the SiGe top layer is completely amorphous, clearly indicating that in this case the whole SiGe layer was melt by the anneal, leaving no seed for a perfect recrystallization. The threshold energy for surface melt is therefore located between 0.76 and 0.79 J/cm^2 and a rapid transition

between a “no melt” and a “full melt” configuration occurs in this small energy interval.

Figure 5 reports the corresponding sheet-resistance measurements as a function of energy densities, which illustrates two different behaviours. Below 0.74 J/cm^2, the sheet-resistance remains below 10 kΩ/sq., with a slight improvement occurring when the energy density is increased (~6000 Ω/sq. after LTA at 0.74 J/cm^2). This indicates that, although the laser anneal did not melt the sample surface, a non-negligible dopant activation occurs at these energies, as it will be discussed below. In contrast, a much higher sheet resistance value (~55 kΩ/sq.) is measured in the sample annealed at 0.77 J/cm^2. Considering that the transition between “no melt” and “full melt” of the 6 nm-thick SiGe layer occurs between 0.76 and 0.79 J/cm^2, the high sheet resistance value measured at 0.77 J/cm^2 suggests that a “full melt” of the SiGe layer has already occurred at this energy and that most of the dopant activation is therefore lost. This behavior is similar to that observed by Acosta et al. [43] in 22 nm-thick Phosphorus-doped SOI, where the sudden increase in the sheet resistance values observed for high laser energies was due to the formation of a poly-Si layer as a consequence of the full melt of the entire top-Si layer during LTA.

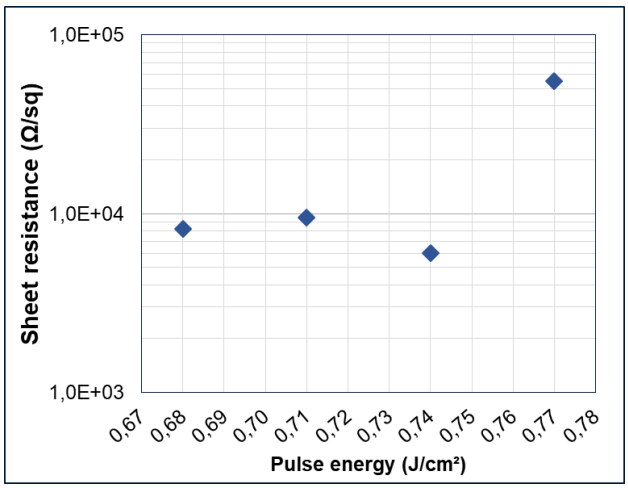

Figure 5: Sheet resistance measurements as function of the laser energy density for a 6nm SiGeOI (x_{Ge}: 0.25 at. %) layer implanted with boron.

For LTA energies lower than 0.74 J/cm^2 (i.e. below the melt threshold) some dopant activation occurs, however the Hall effect measurements indicate that only a small fraction of the implanted Boron dose is electrically active (between 6 and 12%). Two mechanisms contribute to this result: *(i)* the weak dopant penetration through the Si_3N_4 capping layer during the implant and *(ii)* the low activation rate due to the "non-melt" nature of the LTA in this energy range.

In order to investigate the first point, we calculated by SRIM the depth distribution of the Boron implanted ions according to the process conditions used in this experiment. The simulation results indicate that only ~45 % of the Boron implanted dose is available for electrical activation during LTA, the rest being lost in the Si_3N_4 capping layer or in the underlying BOX. Still, the Boron dose contained in the SiGe layer after the implant (~1.8x10^{14} cm^{-2}) is much higher than the electrically active dose actually measured by Hall effect (2.3x10^{13} cm^{-2} after LTA at 0.68 or 0.71 J/cm^2). In addition to this "dose loss" mechanism during implant, a low dopant activation must also occur during LTA.

Indeed, previous investigations [15,44] of dopant activation indicated that in similar conditions, i.e. non-amorphising implants and low thermal budget anneals (either conventional RTA or non-melt LTA), the total active dose (measured from SRP profiles) is much lower than the total implanted dose (as measured by SIMS profiles). However, the few electrically active dopants presents after anneal were not found to be uniformly distributed in depth but rather mostly located close to the surface, where the damage recovery (i.e. interstitial recombination) is favoured (cf. **Supporting Information File 11**). Moreover, even for the smallest thermal budgets (short RTA time or minimum number of laser shots), dopant activation at the surface was maximum or close to the solubility limit at the annealing temperature. Finally, it was

found that dopant activation increases with annealing time despite no dopant diffusion is detected by SIMS.

It is therefore important to verify if this behaviour also occurs in the case of ultra-thin laser annealed SiGeOI samples. Indeed, within the application of laser annealing in contact resistance reduction strategies, such a result may constitutes a strong step forward. One of the LTA samples investigated in this work has therefore been analysed by the Differential Hall effect technique, and results are presented in the next section.

Differential Hall effect analysis

The SiGeOI sample implanted with Boron and annealed with an energy density of 0.68 J/cm^2 was used for this investigations. Four successive SC1 etching processes has been performed for a total etching time of 30, 50, 70 and 90 minutes, reducing respectively the total thickness by 0.1, 0.3, 0.8 and 1.3 nm (confirmed by ellipsometry measurements and TEM images). Concerning surface roughness, TEM images dos not show significant surface roughness, indicating that the surface quality is not degraded by the etch process. This was confirmed by AFM analysis on 500 x 500 nm^2 areas taken from the Van der Pauw sample used for the Hall effect measurements after the longest etch process (90 minutes, cf. **Supporting Information File 12**). Compared to the non-etched region (average roughness of 0.18 nm), the surface roughness is slightly higher in the etched regions (between 0.26 and 0.34 nm) but always much smaller than the total etched thickness (1.3 nm in this sample). Considering that these measurements were performed after the longest etch process and that the surface roughness increases with etching time, we can conclude that the surface roughness induced by the etch process is always negligible and is not expected to have an impact on the reliability of the Hall effect measurements.

The results of the Hall effect measurements (raw data R_s, N_H and μ_H) performed before etch and after each removal step are reported in **Figure 7** as a function of the removed thickness. It appears that the sheet resistance R_S increases very rapidly after each step, with the R_S values increasing by a factor 4 between the second and the third etch step. In fact, only the points corresponding to the three first etch steps are reported in the figure. Following the fourth and longest etch process (1.3 nm removed thickness) the sample was so resistive that quantitative values could not be measured. Correspondingly, the Hall dose N_H is found to rapidly decrease as the etch progresses, qualitatively indicating that most of the active dose is located close to the surface.

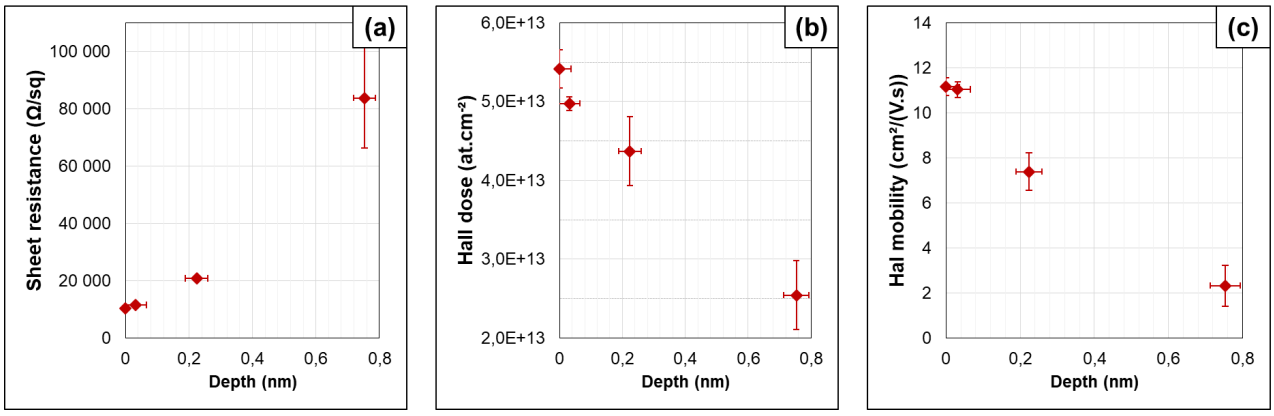

Figure 7: Hall effect measurements (raw data: **(a)** R_s, **(b)** N_H and **(c)** μ_H) from the SiGeOI sample (x_{Ge}: 0.25 at. %) implanted with Boron and annealed at an energy of 0,68 J/cm^2, as a function of the etched thickness (as measured by ellipsometry).

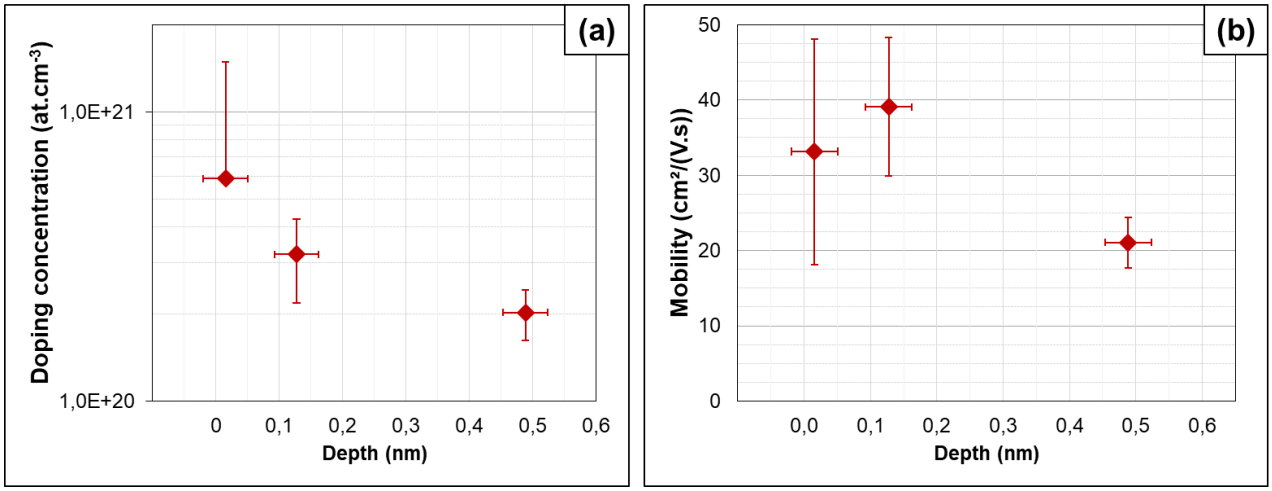

Figure 8: Active dopant concentration **(a)** and carrier mobility **(b)** depth profiles as extracted by DHE method for a SiGeOI sample (x_{Ge}: 0.25 at. %) implanted with Boron and annealed at an energy of 0,68 J/cm^2.

Following the differential Hall data treatment method discussed in previous sections, the depth distributions of the active dopant concentration and of the carrier mobility have finally been extracted and are reported in **Figure 8**. The data quantitatively confirm the results suggested by the Hall effect raw data: the active dopant concentration is highest at the surface with a value as high as ~6x10^{20} cm^{-3} and it rapidly decreases within the first nanometer below the surface (2x10^{20} cm^{-3} at 0.8 nm).

This result is in agreement with the scenario discussed in previous section. Indeed, due to the “non-melt” nature of the anneal, and considering that no amorphisation of the surface was achieved during the implant, the extremely low thermal budget provided by the LTA process is not efficient in removing the implant damage in the material, except in the surface region where the interstitial recombination (and hence damage recovery) is favoured. As a consequence, below the surface, not only the active dopant concentration is much lower than at the surface, but also the residual damage is extremely high, which is expected to have an impact on the carrier

mobility. This is clearly confirmed by the Hall mobility depth profile (cf. **Figure 8b**), whose value at a depth of 0.8 nm below the surface (~20 $cm^2/(V\ s)$) is much lower than the carrier mobility at the surface (~35 $cm^2/(V\ s)$), and this in spite of a much lower carrier concentration. Alternative mechanisms at the origin of such mobility reduction below the surface can be excluded, including surface roughness (cf. **Supporting Information File 12**), and surface depletion due to interface states (cf. previous sections).

In any case, although the investigated doping process is at a preliminary stage, the detailed investigation carried out in this work allows us to conclude that a doping process based on nanosecond laser annealing can be successfully applied to ultrathin SiGeOI layers of ~6 nm thickness, with achieved active dopant concentrations at the surface well above $1x10^{20}$ cm^{-3}. This is a promising result in view of improving contact resistivity in source/drain regions of advanced devices.

Study of 11nm arsenic-doped SOI layer

In the perspective of improving the contact resistance within FDSOI technology [5], different annealing methods are investigated for the increase of dopant activation close to the surface. In this section we will focus on the comparison between conventional spike Rapid Thermal Annealing (RTA) and millisecond laser Dynamic Surface Anneal (DSA), both applied to 11 nm-thick n-type doped SOI layers. In addition to SIMS, TEM and conventional Hall effect measurements, Differential Hall profiling will be shown to allow a reliable estimation of the dopant activation level within the first nanometres below the silicon surface.

Experimental details

Two 11 nm-thick SOI wafers were used for this experiment (BOX thickness: 25 nm, as confirmed by ellipsometry). The wafers were implanted with 3 keV As^+ ions to a

dose of $1x10^{14}$ cm^{-2}. The implants were performed through a thin thermal oxide layer (~1 nm-thick) grown on the as-received wafers. Following the implants, each wafer underwent a different annealing process: 1050°C spike RTA under O_2N_2 ambient in one case, 0.3 ms DSA laser anneal under N_2 ambient in the other case.

Chemical profiles and conventional Hall effet measurements

SIMS characterisations were performed after annealing in both samples without stripping the thermal oxide. The results are shown in **Figure 9** for both Arsenic **(Figure 9a)** and Oxygen (**Figure 9b**). The As concentration profile of the RTA annealed wafer exhibits a peak value of ~$3x10^{20}$ cm^{-3} just below the surface, followed by a quasi-plateau (between 6 and $7x10^{19}$ cm^{-3}) in the rest of the Si top layer. In contrast, the As profile of the DSA wafer is closer to a gaussian shape, with a peak concentration of ~$2x10^{20}$ cm^{-3} at a depth of ~3 nm. In both cases, the sharp decrease of the As concentration below 11 nm corresponds to the transition from the Si top layer to the buried oxide. Similarly, the As signal in the first nm below the surface originates from the dopant atoms contained in the thermal oxide formed prior to the implant. It is therefore critically important to localise the actual position of the oxide/top Si interface in view of the reliable interpretation of the Hall effect data in terms of dopant activation efficiency (i.e. estimation of the active dopant fraction). To this purpose, we used the oxygen SIMS concentration profiles (cf. **Figure 9b**) to estimate the position of the oxide/top Si and of the top Si/BOX interfaces in correspondence of the maximum slope of the oxygen signal. The position of the SiO_2/Si interfaces determined in this way (1.2 nm and 1.6 nm below the surface for the DSA and RTA annealed wafers, respectively) are in perfect agreement with those found by STEM-EDX measurements carried out using an aberration corrected TEM instrument (cf. **Supporting Information File 13** for the RTA annealed wafer) and are reported as dashed lines in **Figure 9**.

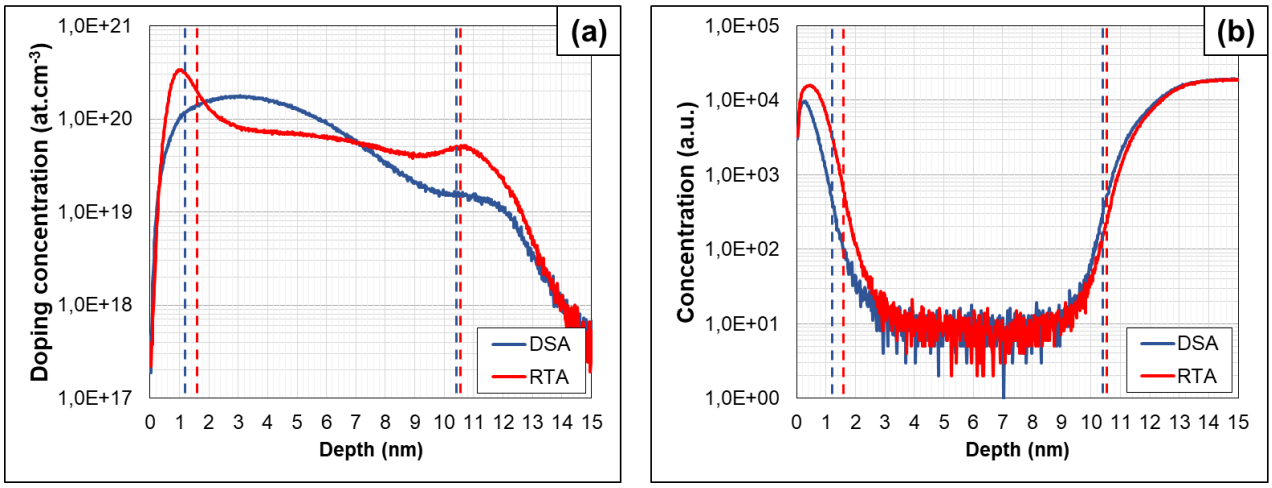

Figure 9: Arsenic **(a)** and Oxygen **(b)** concentration depth profiles measured by SIMS from 11 nm-thick SOI wafers implanted with Arsenic and annealed by RTA (red curves) or DSA (blue curves).

Conventional Hall effect measurements were performed on both annealed wafers and are reported in **Table 1** (a scattering factor r_H = 1 was taken in this case [20]). The results indicate that both anneals provide high dopant activation, with millisecond DSA anneal resulting in slighlty better parameters, i.e. a higher active dopant density and an overall lower sheet resistance compared to spike RTA. Indeed, using the analysis method described in ref. [13] and taking into account the exact location of the SiO_2Si interfaces (as described above), we found that ~92 % of the arsenic ions retained in the top Si layer are electrically active in the DSA annealed wafer, with a maximum active concentration of ~1.4 x 10^{20} cm^{-3}, compared to ~75 % and ~6 x 10^{19} cm^{-3}, respectively, in the RTA wafer. However, these average values do not give access to the actual dopant concentration levels in the surface region. DHE profiling method was therefore used to scan surface doping concentration in both investigated wafers.

Anneal	R_s (Ω/sq)	N_H (at cm^{-2})	μ_H ($cm^2 V^{-1} s^{-1}$)
RTA	2157	4.5×10^{13}	65
DSA	1643	7.8×10^{13}	49

Table 1: Hall effect data measured from 11 nm-thick SOI wafers implanted with As^+ (3 keV, $1x10^{14}$ cm^{-3}) and annealed with spike RTA or millisecon DSA.

Differential Hall effect

For these measurements, after each removal step (based on HF/ethanol cycle) the Van der Pauw test structures were left in a clean room environment from one to three days, so to provide reproducible native oxide regrowth. In order to collect a maximum number of data, we performed thickness and Hall effect measurements before and after oxide stripping. However, considering the possible difference in the surface electrostatic configuration (i.e. the number of interface states) between samples with a stable grown oxide and samples measured just after native oxide stripping, and the impact of the electrostatics on the reproducibility of the Hall effect measurements (cf. **Figure 4a** and related discussion), the DHE data treatment was therefore applied separately to the two sample groups: those measured just after oxide stripping and those measured in the presence of a stable native oxide.

Four successive etching processes were realised for each sample resulting in eight experimental points. All the raw Hall data from both investigated samples are reported in **Figure 10**. When the layer thickness decreases, the electrical parameters evolve following the expected behaviour, with the sheet resistance increasing and the active Hall dose decreasing as a function of the removed thickness. However, due to non-uniformity of the dopant distribution in depth, the observed variations are not linear. As for the carrier mobility, the RTA annealed samples exhibits higher values

with respect to the DSA one, in agreement with the lower active dopant concentration already inferred from conventional Hall measurements (cf. **Table 1**).

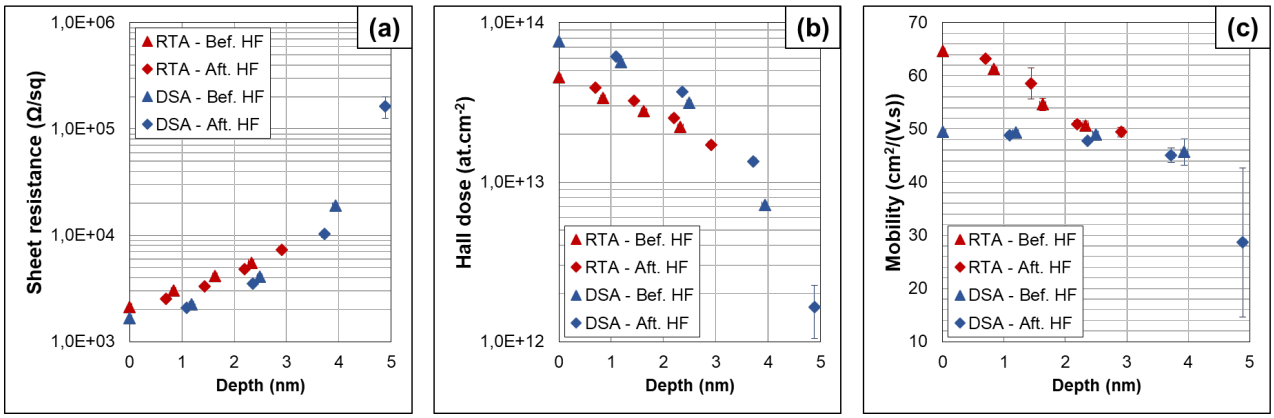

Figure 10: Hall effect measurements (raw data: **(a)** R_S, **(b)** N_H and **(c)** μ_H) from the SOI sample implanted with Arsenic and annealed with DSA (red symbols) and RTA at 1050°C (blue symbols), as a function of the etched thickness (as measured by ellipsometry).

The calculated differential Hall values are finally presented in **Figure 11**. The obtained values are plotted together with arsenic concentration profiles measured by SIMS, by taking into account the actual position of the SiO_2/top Si interface (cf. **Figure 9**). The DHE carrier concentration profiles perfectly follow the chemical profiles measured by SIMS, confirming that both anneal methods provide a high dopant activation efficiency. More importantly, DHE measurements unambiguously show that, within the first two nanometres below the surface, millisecond annealing results in a higher active dopant concentration compared to RTA, making DSA a better candidate than RTA for contact resistance reduction in future FDSOI technologies.

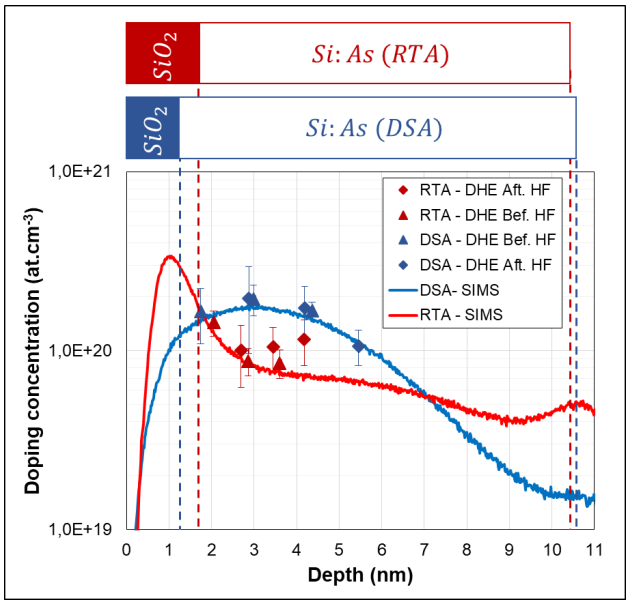

Figure 11: Active dopant concentration depth profiles as extracted by DHE method from 11 nm-thick SOI wafers implanted with As^+ (3 keV, $1x10^{14}$ cm^{-3}) and annealed with spike RTA (red symbols) or millisecon DSA (blue symbols). DHE values are compared with the corresponding Arsenic chemical concentration profiles as measured by SIMS.

Conclusion (optional)

In this paper, we presented an enhanced Differential Hall Effect method that allows to determine, with sub-nm resolution, the level of dopant activation close to the surface for Si and SiGe. In the case of SiGe case, which constitutes the most challenging process, we showed the reliability of the SC1 chemical solution thanks to its slow etch rate, stoichiometry conservation and low roughness generation. For both materials, our method include a direct measurement of the removed thickness after each removal step, so to avoid averaging the etch rate and improve the depth resolution. Then, we demonstrated the reliability of a complete DHE procedure, with an etching step as small as 0.5 nm, on a dedicated 20 nm-thick SiGe test structure fabricated by CVD and uniformly doped *in situ* with boron during growth.

The developed method was finally applied to the investigation of dopant activation achieved by advanced annealing methods in two material systems: 6 nm-thick SiGeOI and 11 nm-thick SOI. In the first case, we showed that a doping process based on nanosecond laser annealing can be successfully applied to ultrathin SiGeOI layers, with achieved active dopant concentrations at the surface well above $1x10^{20}$ cm^{-3}, which is a promising result in view of improving contact resistivity in SiGe source/drain regions of advanced devices. In the second case, DHE measurements unambiguously show that, within the first few nanometres below the surface, millisecond annealing can result in a higher active dopant concentration compared to RTA, making DSA a better candidate than RTA for contact resistance reduction in future FDSOI technologies. In summary, thanks to the improvements implemented in this work, DHE is shown to be a unique sensitive characterisation technique for a detailed investigation of dopant activation in ultra-shallow layers, providing sub-nm resolution for both dopant concentration and carrier mobility depth profiles.

Acknowledgements

This work is partly funded by the French public authorities through the NANO 2017 program. This work has been carried out thanks to French RENATECH network and to the micro and nanotechnologies platform of LAAS-CNRS.

References

1. Doris, B.; DeSalvo, B.; Cheng, K.; Morin, P.; Vinet, M. *Solid-State Electronics* **2016**, 117, 37–59.
2. James, D. *2016 21st International Conference on Ion Implantation Technology (IIT)*, Tainan, Taiwan, September 26–30, 2016.
3. Larrieu, G.; Han, X.-L. *Nanoscale* **2013**, 5, 2437–2441.

4. Batude, P.; Vinet, M.; Xu, C.; Previtali, B.; Tabone, C.; Le Royer, C.; Sanchez, L.; Baud, L.; Brunet, L.; Toffoli, A.; Alain, F.; Lafond, D.; Aussenac, F.; Thomas, O.; Poiroux, T.; Faynot, O. *2011 Symposium on VLSI Technology - Digest of Technical Papers*, Honolulu, HI, USA, June 14–16, 2011.
5. Hutin, L.; Rozeau, O.; Carron, V.; Hartmann, J.-M.; Grenouillet, L.; Borrel, J.; Nemouchi, F.; Barraud, S.; Le Royer, C.; Morand, Y.; Plantier, C.; Batude, P.; Fenouillet-Béranger, C.; Boutry, H.; Ernst, T.; Vinet, M. *2014 International Workshop on Junction Technology (IWJT),* Shanghai, China, May 18–20, 2014.
6. Saraswat, K. C.; Shine, G. *ECS Transactions* **2016**, 75, Issue 8, 513–523.
7. Colombeau, B.; Guo, B.; Gossman, H.-J.; Khaja, F.; Pradhan, N.; Waite, A.; Rao, K. V.; Thomidis, C.; Shim, K.-H.; Henry, T.; Variam, N. *Physica Status Solidi A* **2014**, 211, No. 1, 101–108.
8. Schroder, D. K. Resistivity. *Semiconductor Material and Device Characterization*; Wiley-Interscience: Hoboken, New Jersey, USA, 2006; pp. 29–34.
9. Giannazzo, F.; Raineri, V.; La Magna, A.; Mirabella, S.; Impellizzeri, G.; Piro, A. M.; Priolo, F.; Napolitani, E.; Liotta, S. F. *Journal Of Applied Physics* **2004**, Vol. 97, Issue 1.
10. Giannazzo, F.; Raineri, V.; Mirabella, S.; Bruno, E.; Impellizzeri, G.; Priolo, F. *Materials Science and Engineerings B* **2005**, 124–125, 54–61.
11. Eyben, P.; Janssens, T.; Vandervorst, W. *Materials Science and Engineerings: B* **2005**, 124–125, 45–53.
12. Vandervorst, W.; Fleischmann, C.; Bogdanowicz, J.; Franquet, A.; Celano, U.; Paredis, K.; Budrevich, A. Materials Science in Semiconductor Processing **2017**, 62, 31–48.

13. Severac, F.; Cristiano, F.; Bedel-Pereira, E.; Fazzini, P.-F.; Boucher, J.; Lerch, W.; Hamm, S. *Journal of Applied Physics* **2010**, Vol. 107, Issue 12.
14. Sermage, B.; Essa, Z.; Taleb, N.; Quillec, M.; Aubin, J.; Hartmann, J. M.; Veillerot, M. Journal of Applied Physics **2016**, 119, Issue 15.
15. Fisicaro, G.; Pelaz, L.; Aboy, M.; Lopez, P.; Italia, M.; Huet, K.; Cristiano, F.; Essa, Z.; Yang, Q.; Bedel-Pereira, E. Applied Physics Express, Vol. 7, No. 2, **2014**.
16. Blight, S. R.; Nicholls, R. E.; Sangha, S. P. S.; Kirby, P. B.; Teale, L.; Hiscock, S. P.; Stewart, C. P. *Journal of Physics E: Scientific Instruments* **1988,** 21, No. 5, 470–479.
17. Bennett, N. S.; Smith, A. J.; Colombeau, B.; Gwilliam, R.; Cowern, N. E. B.; Sealy, B. J. *Materials Science and Engineering: B* **2005,** 124–125*,* 305–309.
18. Qin, S.; Prussin, S. A.; Reyes, J.; Hu, Y. J.; McTeer, A. *IEEE Transactions On Plasma Science* **2011,** 39, No. 1, 587–592.
19. Alzanki, T.; Gwilliam, R.; Emerson, N.; Sealy, B. J.; *Applied Physic Letters* **2004,** 85, No. 11, 1979–1980.
20. Bennett, N. S.; Cowern, N. E. B.; Smith, A. J.; Kah, M.; Gwilliam, R. M.; Sealy, B. J.; Noakes, T. C. Q.; Bailey, P.; Giubertoni, D.; Bersani, M. *Materials Science and Engineering: B* **2008,** 154–155*,* 229–233.
21. Ling, Y.-T.; Su, W.-T.; Pi, T.-W; Chang, R.-D.; *AIP Conference Proceedings,* **2012,** Vol. 1496, Issue1.
22. Bennett, N. S.; Cowern, N. E. B. *Applied Physic Letters* **2012,** Vol. 100, Issue 17.
23. LeGoues, F. K.; Rosenberg, R.; Nguyen, T.; Himpsel, F.; Meyerson, B. S. *Journal of Applied Physics* **1989,** 65, Issue 4, pp. 1724–1728.

24. Johnson, F. S.; Miles, D. S.; Grider, D. T.; Wortman, J. J. *Journal of Electronic Materials* **1992,** 21, No. 8, pp. 805–810.

25. Stoffel, M.; Malachias, A.; Merdzhanova, T.; Cavallo, F.; Isella, G.; Chrastina, D.; Von Känel, H.; Rastelli, A.; Schmidt, O. G. *Semiconductor Science and Technology* **2008,** 23, No. 23, pp. 1–6.

26. Gavelle, M. Etude expérimentale de l'interdiffusion Ge-Si à partir de sources solides Germanium sur Silicium - Application à la formation de couches graduelles Si1-xGex pour les transistors pMOSFETs. Ph. D thesis, University of Toulouse, France, **2008**, pp. 168-183.

27. Garrido, B.; Gessinn, F.; Prom, J. L.; Morante, J. R.; Samitier, J.; Sarrabayrousse, G. Silicon Surface Analysis and Very Thin Silicon Oxide Characterization after HF/Ethanol Preoxidation Silicon Cleaning. In, *The Physics and Chemistry of SiO_2 and the Si-SiO_2 Interface 2* Deal, B. E.; Helms, C. R., Eds.; Springer US, US, **1992,** pp. 215–222.

28. Van der Pauw, L. J. *Philips Technical Review* **1958,** 20, No. 8, 220–224.

29. Haeusler, J.; Lippman, H. J. *Solid-State Electronics* **1968,** 11, Issue 1, 173–182.

30. De Mey, G. *Arch. Elektronik und Übertragunstechnik* **1973,** 23, 309–313.

31. David, J. M.; Buehler, M. G. *Solid-State Electronics* **1977,** 20, 539–543.

32. McGregor, J. M.; Manku, T.; Noël, J.-P.; Roulston, D. J.; Nathan, A.; Houghton, D. C. *Journal of Electronic Materials* **1993,** 22, No. 3, 319–321.

33. Carns, T. K.; Tanner, M. O.; Wang, K. L. *Journal of The Electrochemical Society* **1995,** 142, No. 4, 1260–1266.

34. Joelsson, K. B.; Fu, Y.; Ni, W.-X.; Hansson, G. V. *Journal of Applied Physics* **1997,** 81, Issue 3, 1264–1269.

35. Tabe, M.; Kumezawa, M.; Ishikawa, Y. *Japanese Journal of Applied Physics* **2001,** 40, Part 2, No 2B, 131–133.

36. Diarra, M.; Niquet, Y.-M.; Delerue, C.; Allan, G. *Physical Review B* **2007,** 75, 1–4.

37. Björk, M. T.; Schmid, H.; Knoch, J.; Riel, H.; Riess, W. *Nature Nanotechnology* **2009,** 4, 103–107.

38. Pasini, L.; Batude, P.; Lacord, J.; Casse, M.; Mathieu, B.; Sklenard, B.; Piegas Luce, F.; Micout, J.; Payet, A.; Mazen, F.; Besson, P.; Ghegin, E.; Borrel, J.; Daubriac, R.; Hutin, L.; Blachier, D.; Barge, D.; Chhun, S.; Mazzocchi, V.; Cros, A.; Barnes, J.-P.; Saghi, Z.; Delaye, V.; Rambal, N.; Lapras, V.; Mazurier, J.; Weber, O.; Andrieu, F.; Brunet, L.; Fenouillet-Beranger, C.; Rafhay, Q.; Ghibaudo, G.; Cristiano, F.; Haond, M.; Boeuf, F.; Vinet, M. *2016 IEEE Symposium on VLSI Technology,* Honolulu, HI, USA, June 14–16, 2016.

39. Pasini, L. Optimisation des jonctions de dispositifs (FDSOI, TriGate) fabriqués à faible température pour l'intégration 3D séquentielle, Ph. D thesis, University of Grenoble Alpes, France, 2016, 88–96.

40. Kooi, E. *The surface properties of oxidized silicon*; Eindhoven: Technische Hogeschool Eindhoven*,* **1967,** pp. 5–9.

41. Yeo, Y. K.; Hengehold, R. L. *Journal of Appied Physics* **1987**, 61, Issue 11, 5070–5075.

42. TCAD Sentaurus Process User Guide, I-2013.12 version, Synopsis, Inc.: Mountain View, California, USA, 2013.

43. Acosta, P. A.; Kerdilès, S.; Mathieu, B.; Kachtouli, R.; Besson, P.; Veillerot, M.; Aussenac, F.; Fenouillet-Béranger, C.; *2016 21st International Conference on Ion Implantation Technology (IIT),* Tainan, Taiwan, September 26–30, **2016**.

44. Hebras, X. Contributions à l'étude de la diffusion, de l'agglomération et de l'activation du Bore dans le Silicium : Application à la réalisation de jonctions

ultraminces P+/N, Ph.D. Thesis, University of Toulouse, France, **2003,** pp. 127-138.